

## Article

# Step-by-Step Modeling and Experimental Study on the Sol–Gel Porous Structure of Percolation Nanoclusters

Irina Kononova <sup>1</sup>, Pavel Kononov <sup>2,\*</sup>  and Vyacheslav Moshnikov <sup>1</sup> 

<sup>1</sup> Department of Micro- and Nanoelectronics, Faculty of Electronics, Saint-Petersburg Electrotechnical University “LETI”, 197022 Saint-Petersburg, Russia

<sup>2</sup> Department of Descriptive Geometry and Graphics, Faculty of Basic and Human Sciences, Saint-Petersburg Mining University, 199106 Saint-Petersburg, Russia

\* Correspondence: kononov\_pv@pers.spmi.ru; Tel.: +7-981-201-5259

**Abstract:** Non-conventional crystallization techniques have been developed in recent years. Non-conventional crystallization techniques use primary structural elements (for example, clusters) rather than atoms and molecules. Modern nanomaterial science is going through great changes as an entirely new approach of non-conventional growth mechanisms is emerging due to cluster coupling, catalyzing interest in cluster physics. The formation of fractal and percolation clusters has increased. We carried out step-by-step modeling and an experimental study of the formation of fractal and percolation clusters based on tin dioxide and silicon dioxide and formed by sol–gel technology. In this paper, the growth of fractal aggregates (clusters) from sol particles SnO<sub>2</sub> and SiO<sub>2</sub> based on the modified models of diffusion-limited and cluster–cluster aggregation is discussed. A percolation model using simulated fractal clusters of SnO<sub>2</sub> and SiO<sub>2</sub> particles is proposed. Experimental data on the sol–gel percolation structure of porous nanocomposites are presented. The modeling of SnO<sub>2</sub> and SiO<sub>2</sub> particles, which also consist of clusters (the next step in the hierarchy), is shown. We propose a generalized hierarchical three-dimensional percolation cluster model that allows calculating the surface area, knowing the experimental sizes of macropores and taking into account the micro- and mesopores (sizes less than a few nanometers).

**Keywords:** sol–gel films; computer modeling; micro-, meso- and macropores; dioxide tin; dioxide silica



**Citation:** Kononova, I.; Kononov, P.; Moshnikov, V. Step-by-Step Modeling and Experimental Study on the Sol–Gel Porous Structure of Percolation Nanoclusters. *Coatings* **2023**, *13*, 449. <https://doi.org/10.3390/coatings13020449>

Academic Editor: Peter Rodič

Received: 30 December 2022

Revised: 8 February 2023

Accepted: 9 February 2023

Published: 16 February 2023



**Copyright:** © 2023 by the authors. Licensee MDPI, Basel, Switzerland. This article is an open access article distributed under the terms and conditions of the Creative Commons Attribution (CC BY) license (<https://creativecommons.org/licenses/by/4.0/>).

## 1. Introduction

Non-conventional crystallization techniques, including oriented attachment [1–3] as well as mesocrystals [4] and mesocrystals with mineral bridges [5], have been developed in recent years.

A common feature of these new non-traditional crystallization mechanisms is the use of primary structural elements rather than atoms and molecules. An example of using polyatomic primary elements is the development of clathrate physics, this field being especially relevant for the new generation of thermoelectric materials. Clathrates for thermoelectricity were proposed in the 1990s and were termed “phonon glass–electronic crystal”. The essence of this concept is to create a highly conductive shell of hollow elements and fill the inner volume of the clathrate with chemically unbound atoms that would ensure a reduction in thermal conductivity due to phonon scattering. This results in increased thermoelectric efficiency [6].

Typical examples of structures made up of primary structural elements are zeolites [7]. Quasicrystals have recently been actively studied. As it was shown in [8–10], the structure of icosahedral quasicrystals can be described without using the six-dimensional space geometry. The Madison four-body model allows the structure of four types of unit cells to be constructed while filling the space with identical copies of the unit cells according to the self-similarity principle rather than the translational invariance. In addition,

algorithms for the atom arrangement at the cell interface have been developed. The multicell approach was proposed.

There are other examples of practical application of structural elements in modern nanomaterials [11–15] in the form of a polyhedra of one or more types.

As it follows from the above, a relevant task of scientific and practical interest is to develop the sections related to formation of polyhedral nanocrystals, the connection between the morphology of nano-objects and their size, as well as the transition of morphological forms into each other in accordance with the minimum energy principle.

Modern nanomaterial science [16–24] is going through great changes as an entirely new approach of non-conventional growth mechanisms is emerging due to cluster coupling. Non-conventional crystallization incorporates processes that are not governed by the condition that only orders 1, 2, 3, 4 and 6 of symmetry should exist, and since not an infinitely solid body is considered, orders 5, etc., can also exist, so energy forms are considered that are favorable with respect to various symmetry axes. Whereas previously, all issues related to the expansion of atoms were considered, nowadays more and more attention is focused on the possibility of engaging the attachment mechanisms and obtaining mesocrystals.

Interest in cluster physics increased in the late 20th century, when a new term “cluster” was coined [25–29], meaning “a group of similar things growing or held together”. The concept of “clusters” [28,29] is becoming ever more relevant due to the recent trend in the development of nanomaterials.

Nanomaterials obtained using non-conventional growth mechanisms are of extreme interest [25–29] in the field of electronics and photonics, as well as in catalysis. For example, a new class of materials, i.e., the “phonon glass-electron crystal”, opens a new chapter in thermoelectric materials science.

Nanoclusters and nanocrystals are known to be nanosized complexes of atoms or molecules. The main difference between them lies in the way their constituent atoms or molecules are arranged, as well as the chemical bonds between them. In terms of the degree of their structural order, nanoclusters are subdivided into ordered, otherwise known as magic, and unordered.

The formation of fractal and percolation clusters is also of interest. Recently, fractal and percolation clusters [30–33] were formed in sol–gel processes [34,35].

Fractal clusters [36,37] can form in sol–gel technology. Such systems have a branched structure and are formed in a large number of physical processes accompanied by the association of solid particles of similar sizes. When sol–gel nanocomposites are obtained, it is possible to form a percolation cluster with a fractal structure.

Percolation and fractal clusters differ in nature. A percolation cluster occurs in the matrix only when the concentration of particles in its composition increases above a certain threshold of flow. The density of an infinite percolation cluster must exceed a certain critical value. In the case of a fractal cluster, it can be arbitrarily small.

The products of sol–gel technology [38–43] in microelectronics, as a rule, are layers onto which the requirements of smoothness, continuity and uniformity in composition are imposed. For gas-sensitive sensors of a new generation, technological methods for obtaining porous [44] nanocomposite layers with percolation structure and controlled and reproducible pore sizes are of greater interest. At the same time, nanocomposites must contain a phase to improve adhesion and one or more phases of *n*-type semiconductor metal oxides of electrical conductivity to ensure gas sensitivity.

The aim of the work was step-by-step modeling and experimental study of the formation of a percolation cluster based on tin dioxide and silicon dioxide and formed by sol–gel technology: modeling of the growth of fractal aggregates (clusters) from sol particles SnO<sub>2</sub> and SiO<sub>2</sub> using modified models of diffusion-limited and cluster–cluster aggregation; creation of the percolation model using simulated fractal clusters of SnO<sub>2</sub> and SiO<sub>2</sub> particles; obtaining experimental data on the sol–gel percolation structure of porous nanocomposites; modeling of SnO<sub>2</sub> and SiO<sub>2</sub> particles, which in turn also consist of clusters (the next step in the hierarchy); creation of a generalized hierarchical three-dimensional percolation cluster

model allowing calculating the surface area, knowing the experimental sizes of macropores and taking into account the micro- and mesopores (sizes less than a few nanometers).

## 2. Materials and Methods

Materials based on  $\text{SiO}_2$ ,  $\text{SnO}_2$  and produced by sol–gel synthesis were investigated in this study. The source of  $\text{SiO}_2$  was  $\text{Si}(\text{OC}_2\text{H}_5)_4$  (tetraethoxysilane, TU2637-187-44493179-2014, Moscow, Russia), and the source of  $\text{SnO}_2$  was  $\text{SnCl}_2 \cdot 2\text{H}_2\text{O}$  (GOST 36-78, Saint-Petersburg, Russia). Films were produced from sols by spin casting.

The atomic force microscopy and electron microscopy were used to investigate film materials.

A modified Witten–Sander model for a two-component system and a modified cluster–cluster aggregation model were proposed using the program Microsoft Visual C++ 2013 and Processor Intel core i5 (calculation times were several tens of seconds).

Three-dimensional modeling of nanostructures was performed with Autodesk 3ds Max 2019.

## 3. Results

### 3.1. The Growth of Fractal Aggregates (Clusters) from Sol Particles $\text{SnO}_2$ and $\text{SiO}_2$ Based on the Modified Models of Diffusion-Limited and Cluster–Cluster Aggregation

The growth model of fractal aggregates in ash refers to the model of diffusion-limited aggregation (DLA or Witten–Sander model). Computer experiments based on the modified DLA model were performed on a two-dimensional (triangular) lattice. Within the framework of the model, each particle started from a randomly selected point on a large circle centered in the embryo. In calculations, the number of points on the large circle varied from 4 to 20. The probability of adhesion of a particle was set to 100%, in the second coordination sphere, 50%, and in the third coordination sphere, 25%. Since sols were obtained using two precursors,  $\text{Si}(\text{OC}_2\text{H}_5)_4$  and  $\text{SnCl}_2 \cdot 2\text{H}_2\text{O}$ , computer modeling was carried out in a system consisting of two types of particles. The addition of TEOS to an alcoholic solution of an inorganic tin salt was carried out only after the destruction of the structure of the solute ( $\text{SnCl}_2 \cdot 2\text{H}_2\text{O}$ ) and the interaction of the solvent with the solute particles. Therefore, the particles of the second type began to diffuse in space after 50% of the particles of the first type joined the aggregate. As illustrative examples, Figure 1 presents typical simulation results that match the results of the experiment (Figure 2). It is shown that neighboring branches of aggregates can be combined. Fractal branched macromolecules were formed. The side chains interacted and connected. Incorrect grids were formed. The connection was also carried out using short “jumpers” between the circuits.

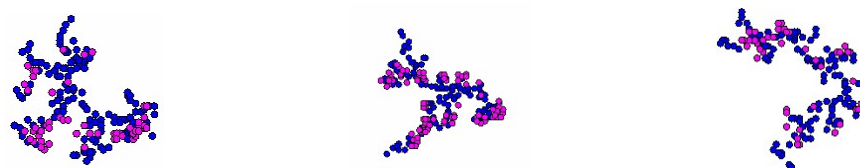


Figure 1. Typical DLA simulation results.

The result of the simulation is a visual observation of fractal changes and an understanding of the possibility of varying the value of the flow threshold. Modeling allowed us to explain the high value of the flow threshold in the experiment. It is shown that the nonconducting phase is formed not only due to the formation of the dielectric-phase  $\text{SiO}_2$ , but also due to the formation of mixed-phase  $\text{SnO}_2$  and  $\text{SiO}_2$ .

As the sol exposure increases, chemical crosslinking reactions occur between branched macromolecules. Computer experiments were carried out using a modified model of cluster–cluster aggregation (CCA), in which the formed clusters perform chaotic motion in solution together with particles. In our generalized model, the processes of DLA and CCA proceed simultaneously. Simultaneous movement of all particles was carried out, and the

movement of clusters was carried out at a speed inversely proportional to their mass. The particles diffused in a limited space according to the CCA. A solid dimer was formed when two particles collided. The dimer also made random wanderings in the ash. This dimer was connected to another dimer or to a separate particle, etc. Two colliding clusters formed a large cluster after the collision. Figure 3 shows typical computer simulation results. The processes are shown in the ash with an increase in the holding time of the solution. A large percolation cluster was forming.

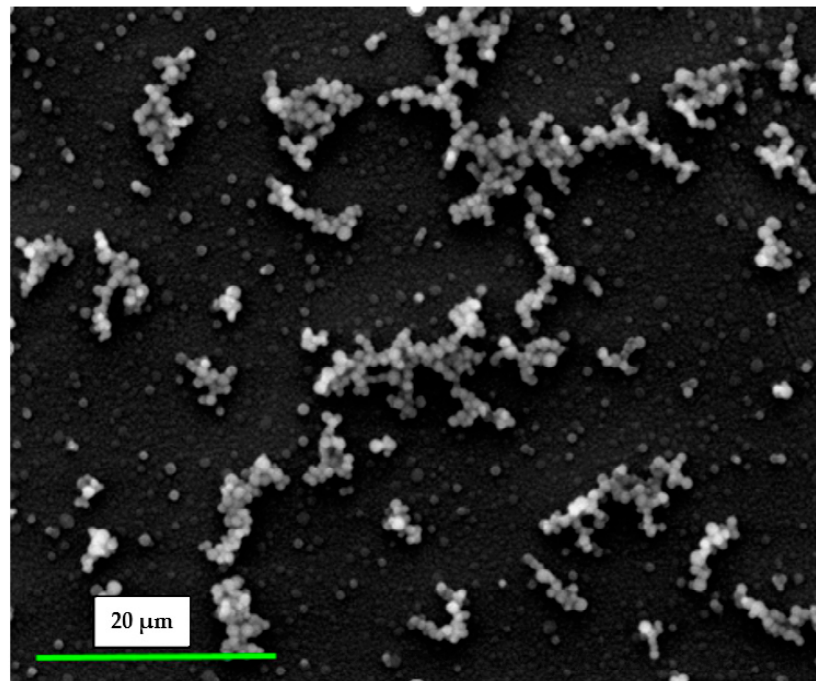


Figure 2. A scanning electronic microscopy image (SiO<sub>2</sub> sample).

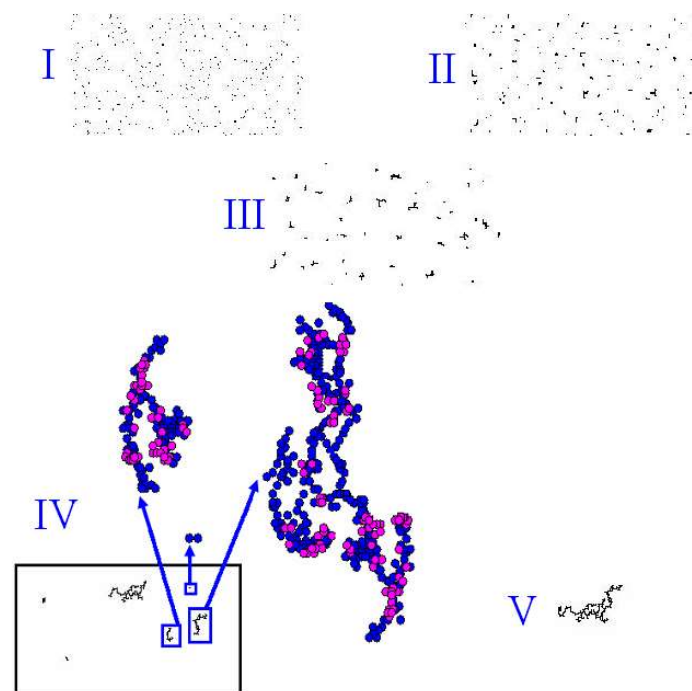


Figure 3. Typical results of the modified CCA model.

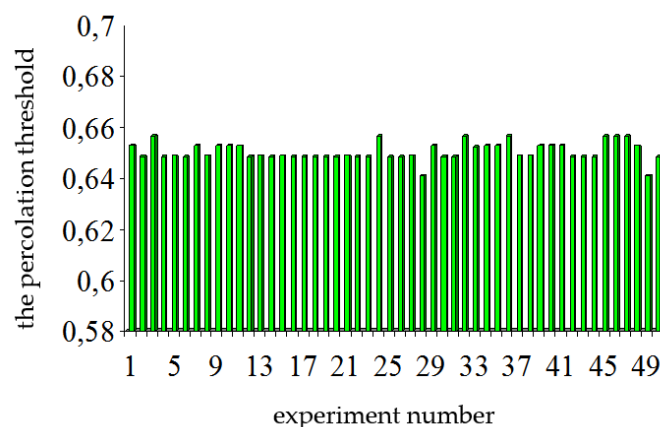
### 3.2. The Percolation Model Using Simulated Fractal Clusters of SnO<sub>2</sub> and SiO<sub>2</sub> Particles

Sol-gel technology products can be objects with a fractal structure, but not belonging to the group of fractal aggregates. These are so-called percolation clusters. The fundamental differences between a fractal aggregate and a percolation cluster are that a fractal aggregate begins to form at arbitrarily small concentrations of particles, and a percolation cluster occurs only when the concentration corresponding to the flow threshold is exceeded. In this work, the flow thresholds were calculated on two-dimensional lattices with specified parameters (node tasks, the number of nodes varied from 100 to 40,000). The software product also implements the capabilities of oriented flow analysis, for example, under conditions of an applied electric field. Since, under the action of a constant electric field, the movement of electrons through conducting grains is carried out only against the field, during calculations, restrictions were imposed on the search for a percolation contracting cluster (geometric phase transition). It was assumed that the composites consisted of two types of grains: conductive based on tin dioxide and non-conductive based on silicon dioxide. An increase in the proportion of grains of the first type in the starting material compared to grains of the second type allows one to change the electrical properties from fully insulating to conductive. Near the threshold of leakage, the body is divided into parts with different properties. It is shown that the geometry of these partitions acquires new random shapes each time, but the values of the flow threshold for bodies of infinite dimensions are strictly defined and depend on the symmetry and dimension of space (Figure 4).



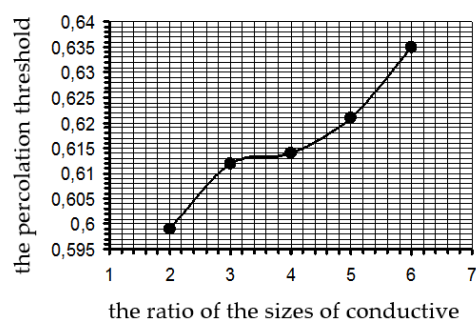
**Figure 4.** Typical illustrations of percolation clusters on a square lattice (22,500 nodes).

Figure 5 shows histograms showing changes in the random value of the percolation threshold in 50 experiments.



**Figure 5.** Histogram of the change in the values of the random value of the percolation threshold.

In the case of predominant formation of SnO<sub>2</sub> fractal aggregates at the initial stages of growth, their sizes exceed those of SiO<sub>2</sub> and mixed particles (SnO<sub>2</sub> and SiO<sub>2</sub>). Therefore, changes in the value of the percolation threshold when using the size ratio of conductive SnO<sub>2</sub> and non-conductive particles (SiO<sub>2</sub> and mixed particles of SnO<sub>2</sub> and SiO<sub>2</sub>) occur (Figure 6).

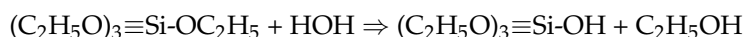


**Figure 6.** Change in the percolation threshold depending on the ratio of the sizes of conductive and non-conductive particles.

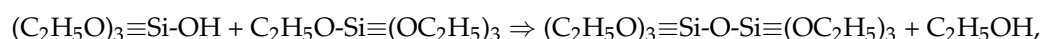
The percolation model on a two-dimensional lattice can also be interpreted as a model of branched polymerization. Imitation of concentrated gel was carried out in the form of colored dots, and that of pure solvent was in the form of white dots (Figure 4). It can be seen that percolation systems represent grids. Heat treatment of nanostructures based on such percolation systems leads to the release of solvent from the grid and the formation of a system of pores, the size of which can be controlled by changing the conditions of sol–gel synthesis.

### 3.3. Experimental Study on the Sol–Gel Percolation Structure of Porous Nanocomposites

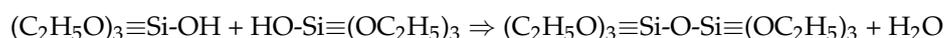
The main sol–gel reactions based on tetraethyl orthosilicate (TEOS, Si(OC<sub>2</sub>H<sub>5</sub>)<sub>4</sub>) are as follows:



and



or



The formation of other organoelement compounds is possible. An example is shown in Figure 7.

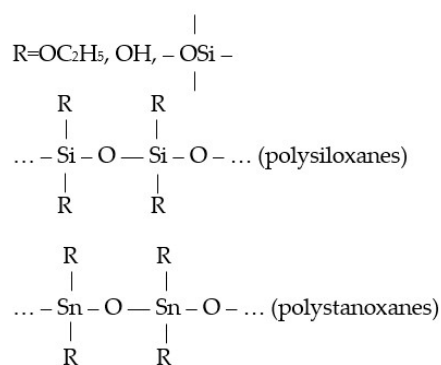


**Figure 7.** Example of organoelement compounds.

Film porous nanocomposites based on tin dioxide and silicon dioxide were obtained from sols based on polystanoxanes and polysiloxanes.

To determine the thickness of nanostructured layers on siall substrates, cross-sections (Figure 8) were created by an acutely focused beam of gallium ions provided by the Strata FIB 205 (focused ion beam microscope).

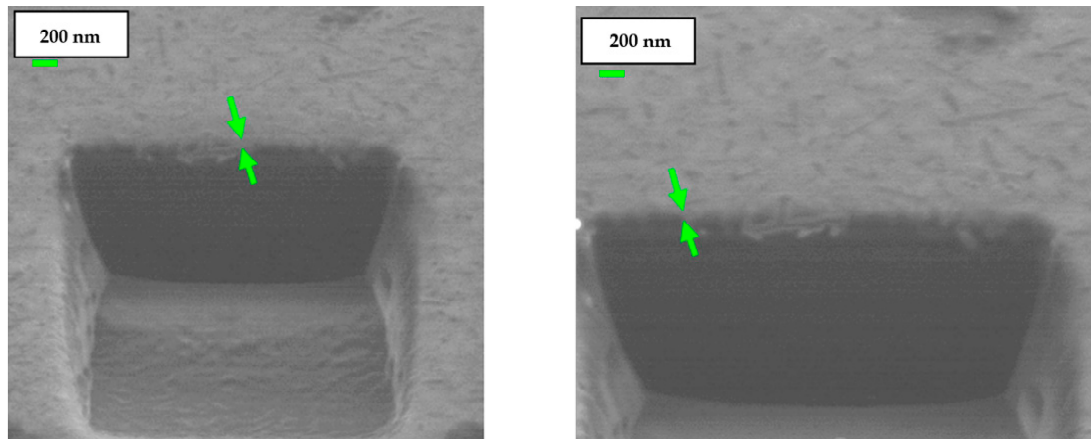


**Figure 8.** Image of the section.

This analytical and technological complex allows local ion beam preparation of complex heterogeneous objects with a spatial resolution of 0.1 microns. To study the sample section, the object table was rotated at an angle of  $45^\circ$ , and the observation was carried out in secondary electrons excited by an ion beam with a diameter of 7 nm. Grooves ( $5 \mu\text{m} \times 5 \mu\text{m}$ , depth  $2 \mu\text{m}$ ) were formed. The thickness of the semiconductor layers (indicated by bright green arrows in Figure 8) is 200 nm.

The transition from theoretical problems (which are reduced to finding the value of flow thresholds for two-dimensional lattices) was made to solve experimental problems of percolation theory in a system based on tin and silicon dioxides (Figures 9–11). The experimental results of the study allowed us to determine the composition of the nanocomposite at which a percolation cluster occurs ( $50 \text{ SiO}_2$ — $50 \text{ SnO}_2$  (mol. %), Figure 11). The percolation cluster is a porous nanomaterial with macropore sizes of 150–200 nm and 350–400 nm (IUPAC recommendation: micropore size—below 2 nm, mesopore size—2–50 nm, macropore size—over 50 nm).

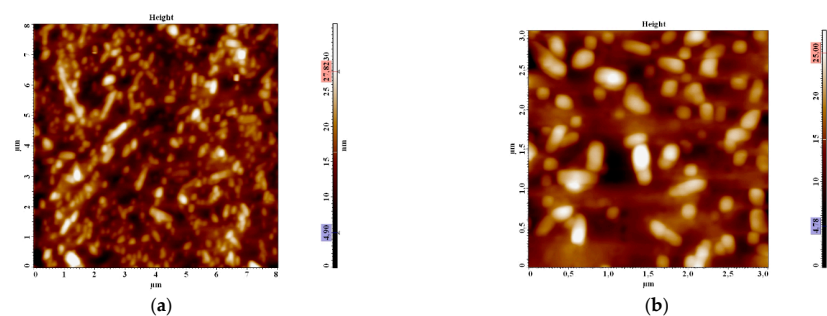


**Figure 9.** AFM image of  $\text{SiO}_2$  film: (a) image size  $8 \mu\text{m} \times 8 \mu\text{m}$ ; (b) image size  $3 \mu\text{m} \times 3 \mu\text{m}$ .

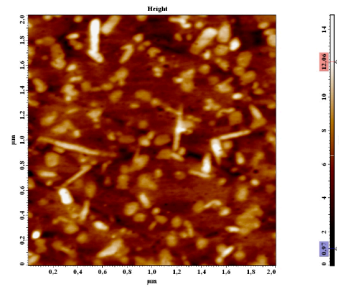


**Figure 10.** AFM image of 60 SiO<sub>2</sub>—40 SnO<sub>2</sub> (mol. %) film, image size 2 μm × 1.8 μm.

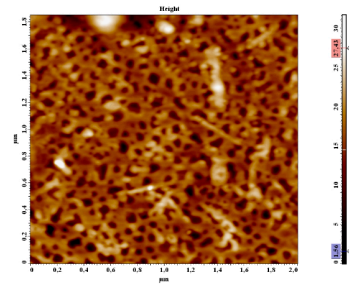


**Figure 11.** AFM image of 50 SiO<sub>2</sub>—50 SnO<sub>2</sub> (mol. %) porous film, image size 2 μm × 1.8 μm.

The value of the flow threshold significantly exceeds (16%) the solution of the classical problem for 3D space. However, the simulation results predict such a deviation due to the initial formation of SnO<sub>2</sub> clusters and changes in the particle size ratio of conducting and non-conducting phases at the stage of cluster–cluster aggregation during the formation of nanocomposites.

It was possible to determine that the conducting branches of the studied percolation structures contain a system of open mesopores of the order of 10 nm in size (Figure 12).

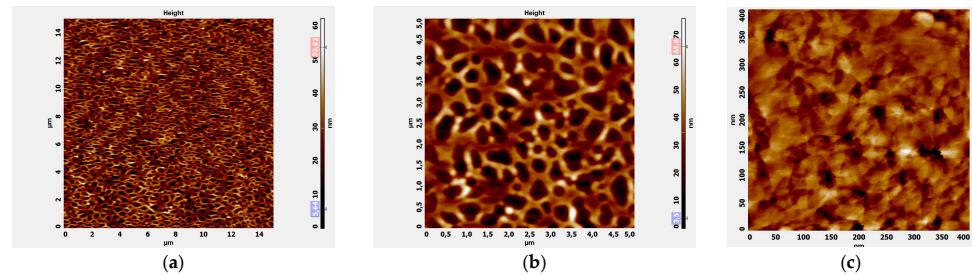


**Figure 12.** AFM image of 80 SiO<sub>2</sub>—20 SnO<sub>2</sub> (mol. %) film: (a) image size 15 μm × 15 μm, (b) image size 5 μm × 5 μm, (c) image size 400 nm × 400 nm.

### 3.4. Generalized Hierarchical Three-Dimensional Percolation Cluster Model

This article proposes a three-dimensional percolation model of the formation of porous hierarchical nanomaterials, limited from below, by applying the film to the substrate. The percolation cluster is a porous nanomaterial with macropore sizes of 150 nm and 400 nm (the first pore type, Figure 13). One of the eleven Kepler nets (Figure 13) with Schläfli symbol no. 4612 [14,33] was used.

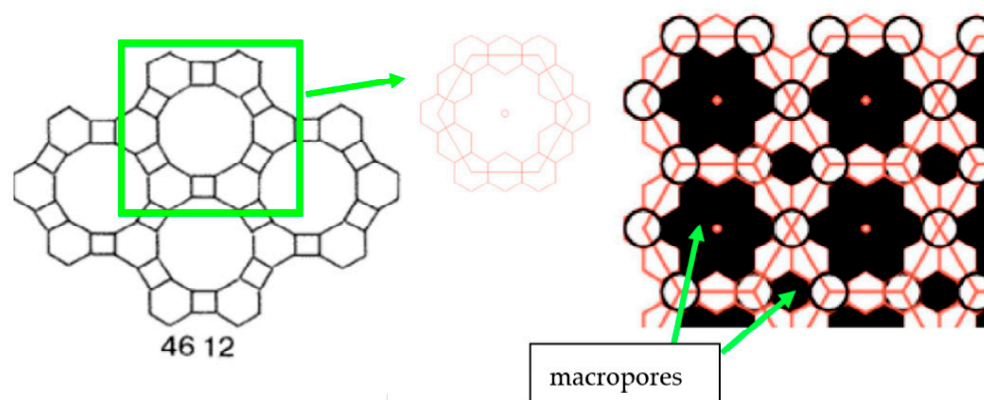


**Figure 13.** One of the eleven Kepler nets with Schläfli symbol no. 4612 and fragment of the enhanced Kepler net of the 4612 type.

A square was replaced by a regular hexagon. Thus, a large hexagon was obtained (Figure 13).

Each regular hexagon in the enhanced Kepler net with the Schläfli 4612 symbol was filled with clusters consisting of SiO<sub>2</sub> and SnO<sub>2</sub> particles. Simulations of SiO<sub>2</sub> and SiO<sub>2</sub> particle clusters are given below.

It should be noted that the results of earlier studies show that the conducting branches of macroporous materials have a hierarchical structure.

### 3.5. Formation of Clusters along the Octahedral Line

Table 1 shows the results of calculating the number of structural units (atoms, molecules) in the original octahedral clusters and in clusters that have been truncated in various ways.

**Table 1.** The results of calculating the number of structural units (atoms, molecules) in the original octahedral clusters.

<i>l</i>	$N_l^{OK}$ at <i>p</i> Values						
	0	1	2	3	4	5	6
1	1						
2	6	0					
3	19	13					
4	44	38	14				
5	85	79	55				
6	146	140	116	62			
7	231		201	147			
8	344		314	260	164		
9	489			405	309		
10	670			586	490	340	
11	891			807	711	561	
12	1156				976	826	610
13	1469				1289	1139	923

The octahedral numbers are also obtained by direct calculation, if we consider that an octahedron with *l* structural units per edge consists of two square pyramids with (*l*−1) structural units per edge, each containing  $N_{l-1}^{II}$  structural units, and a square with  $l^2$  structural units between them.

$$N_{l-1}^{\text{II}} = \sum_{i=1}^{l-1} (i-1)^2 = \frac{1}{6} [(l-1) \cdot l \cdot (2l-1)]$$

Therefore, the octahedral number is calculated using the following equation:

$$N_l^{\text{OK}} = 2N_{l-1}^{\text{II}} + l^2 = \frac{l(2l^2 - l - 2l + 1 + l)}{3}; N_l^{\text{OK}} = \frac{l(2l^2 + 1)}{3} \text{ at } p = 0$$

Figures 14–17 present isometric shapes of crystallographic octahedral clusters with the number of structural units per octahedron edge  $l = 2$  and  $l = 3$  and their axonometric views with a visual representation of all 6 and 19 structural units in the cluster, respectively.

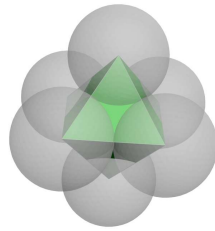


**Figure 14.** Image of a 6-atom octahedral cluster with the number of structural units on the octahedron edge  $l = 2$  (without cutting off at  $p = 0$ ).

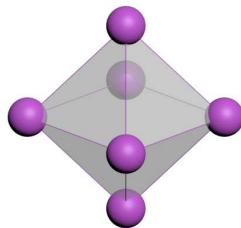


**Figure 15.** Schematic representation of the location of structural units in a 6-atom octahedral cluster, shown in Figure 14.

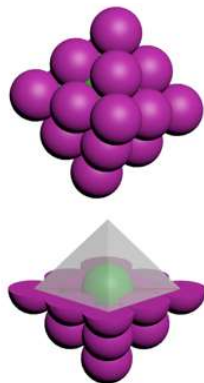


**Figure 16.** Image of a 19-atom octahedral cluster with the number of structural units on the octahedron edge  $l = 3$  (without cutting off at  $p = 0$ ).

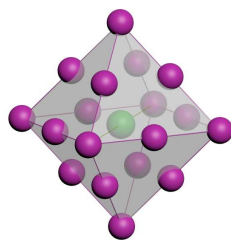


**Figure 17.** Schematic representation of the location of structural units in a 19-atom octahedral cluster, shown in Figure 16.

Modeling in the Autodesk 3ds Max software revealed that eighteen structural units are located on the faces and one structural unit is in the center of the octahedron at the intersection of its three equal diagonals (in the octahedron, all diagonals are equal to each other and perpendicularly intersect in the center in pairs).

If we “round off” an octahedron (Table 1) by cutting off square pyramids with  $p$  structural units per edge ( $p \leq [l/2]$ ) from its six vertices, then the general equation of the “magic numbers” for such configurations will take the following form:

$$N_l^{\text{OK}}(p) = N_l^{\text{OK}} - 6N_p^{\text{II}}$$

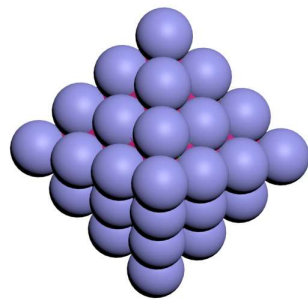
$$p = l - 1 \Rightarrow l = p + 1$$

$$N_p^{\text{II}} = \frac{1}{6}[p \cdot (p + 1) \cdot (2p + 2 - 1)] = \frac{1}{6}[p \cdot (p + 1) \cdot (2p + 1)]$$

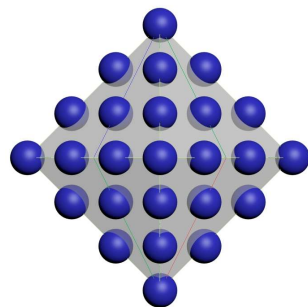
$$N_l^{\text{OK}}(p) = N_l^{\text{OK}} - 6N_p^{\text{II}} = \frac{l(2l^2 + 1)}{3} - [p \cdot (p + 1) \cdot (2p + 1)]$$

$$\text{For example : } N_{l=6}^{\text{OK}}(p = 3) = \frac{6(2 \cdot 6^2 + 1)}{3} - [3 \cdot (3 + 1) \cdot (2 \cdot 3 + 1)] = 146 - 84 = 62$$

Figures 18 and 19 present an image of a 44-atom octahedral cluster with the number of structural units per octahedron edge  $l = 4$  and its schematic representation of the location of structural units in a 44-atom octahedral cluster.

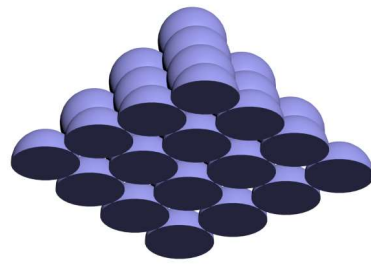


**Figure 18.** Image of a 44-atom octahedral cluster with the number of structural units on the octahedron edge  $l = 4$  (without cutting off at  $p = 0$ ).

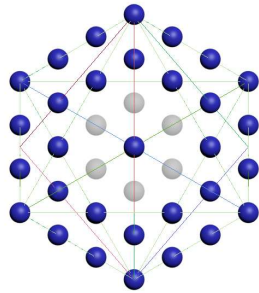


**Figure 19.** Schematic representation of the location of structural units in a 44-atom octahedral cluster, shown in Figure 18.

Figure 20 presents a cross-section of a 44-atom octahedral cluster along the symmetry plane (bottom view), and Figure 21 shows an orthogonal view of a 44-atom octahedral cluster centered by an edge.



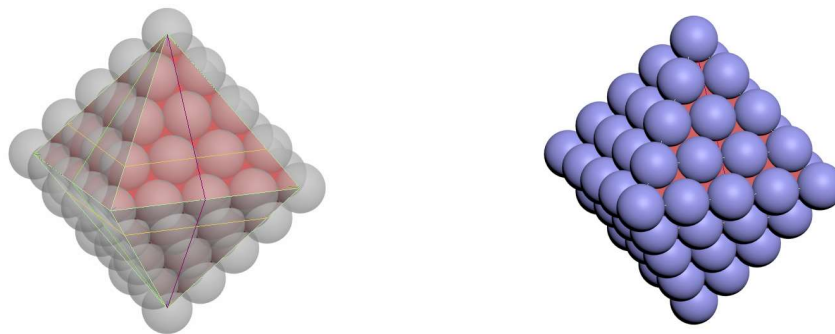
**Figure 20.** A cross-section of a 44-atom octahedral cluster along the symmetry plane (bottom view).



**Figure 21.** Orthogonal view of a 44-atom octahedral cluster centered by an edge.

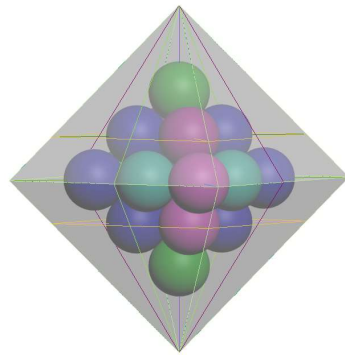
Since 4 structural units are on one octahedral cluster edge, there are 30 structural units on its 12 edges. There is one structural unit in the center of each edge, which makes eight structural units on eight edges of the octahedron. Two structural units are located on each diagonal of the octahedral cluster, so the results of modelling in the Autodesk 3ds Max software show that six structural units are located inside the octahedral cluster on its three diagonals (with no structural unit in the center).

Figure 22 presents an image of an 85-atom octahedral cluster with the number of structural units per octahedron edge  $l = 5$ .



**Figure 22.** Image of an 85-atom octahedral cluster with the number of structural units per the octahedron edge  $l = 5$  (without cuffing off at  $p = 1$ ).

Since 5 structural units are on one octahedral cluster edge, there are 42 structural units on its 12 edges. There are 3 structural units in the center of each edge, which makes 24 structural units on eight edges of the octahedron. Based on the results of modeling in the Autodesk 3ds Max software, it was found that there is a small octahedron with 19 structural units inside the octahedron cluster with the number of structural units per octahedron edge  $l = 5$  (Figure 23). Thus, the result of summing up 42, 24 and 19 structural units produces 85.



**Figure 23.** A visual representation of the internal small octahedron of an 85-atom octahedral cluster, shown in Figure 22.

According to the modeling results, it was established that the number of structural units inside an octahedral cluster ( $L_l$ ) with the number of structural units per the octahedron edge  $l = 3, l = 4, l = 5$  equals  $L_{l=3} = 1, L_{l=4} = 6, L_{l=5} = 19$ , respectively. Therefore, if  $N_l^{OK} = 2N_{l-1}^{II} + l^2 = \frac{l(2l^2+1)}{3}$  *npu*  $p = 0$ , then  $L_l = N_{l-2}^{OK} = \frac{(l-2)(2(l-2)^2+1)}{3}$  *npu*  $p = 0$   $u \ l \geq 3$ . Thus, the dependence of the number of structural units per the octahedron edge  $l$  on the number of structural units inside the octahedral cluster  $L_l$  without cutting off is a cubic function ( $L_l(l) = 0.6667l^3 - 4l^2 + 8.3333l - 6$ ), which is defined by a cubic polynomial (Figure 24).

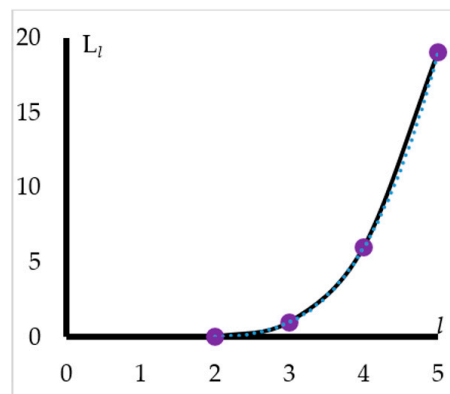


**Figure 24.** The dependence of the number of structural units inside the octahedral cluster  $L_l$  (without cutting off) on the number of structural units per the octahedron edge  $l$ .

Table 2 shows the results of modeling and the dependence of the number of structural units inside the octahedral cluster  $L_l$  on the number of structural units per the octahedron edge  $l$  and the number of structural units in octahedral clusters.

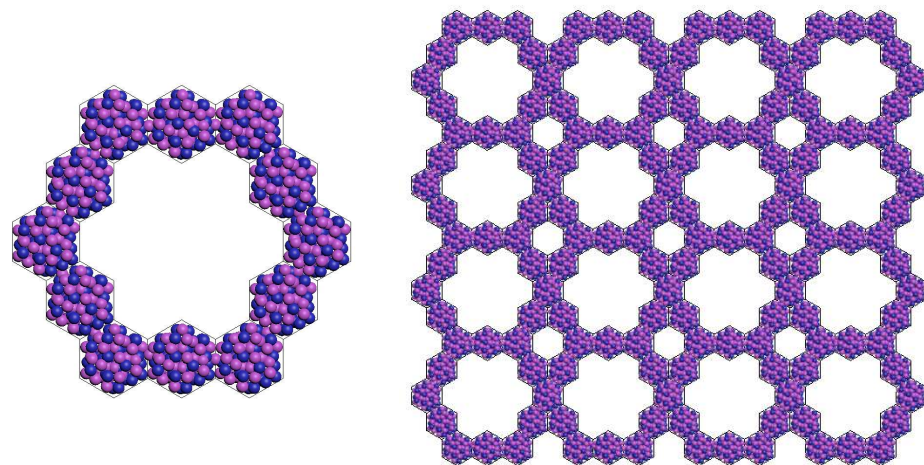
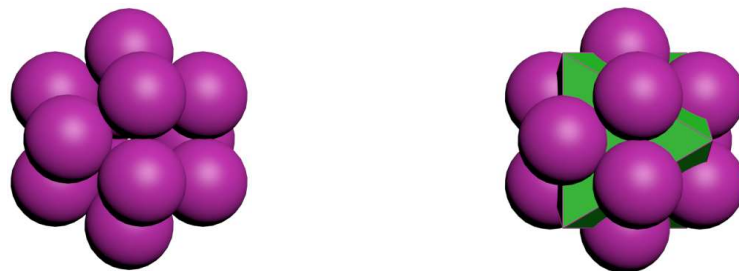
It was established that the dependence of the number of structural units per the octahedron edge on the number of structural units inside the octahedral cluster without cutting off is a cubic function which is defined by a cubic polynomial. A formula is proposed to calculate the number of structural units within an octahedral cluster.

**Table 2.** The number of structural units inside the octahedral cluster.

$l$	$N_l^{OK}(p=0)$	$L_l$
1	1	
2	6	
3	19	1
4	44	6
5	85	19
6	146	44
7	231	85
8	344	146
9	489	231
10	670	344
11	891	489
12	1156	670
13	1469	891

#### 4. Discussion

Each regular hexagon in the enhanced Kepler net with the Schläfli 4612 symbol was filled with upgraded three-dimensional deterministic Julien fractal aggregates (Figure 25). Nonporous identical spherical particles in the Julien fractal cluster were replaced by 13-atom octahedral clusters with the number of structural units per the octahedron edge  $l = 3$  (with cutting off at  $p = 1$ , Figure 26).

**Figure 25.** Fragment and the enhanced Kepler net of the 4612 type with the cells filled.**Figure 26.** Image of a 13-atom octahedral cluster with the number of structural units per the octahedron edge  $l = 3$  (without cuffing off at  $p = 1$ ).

The following three pore types (Figure 27) were observed in the enhanced Kepler net of the 4612 type with cells filled with 13-atom octahedral clusters.

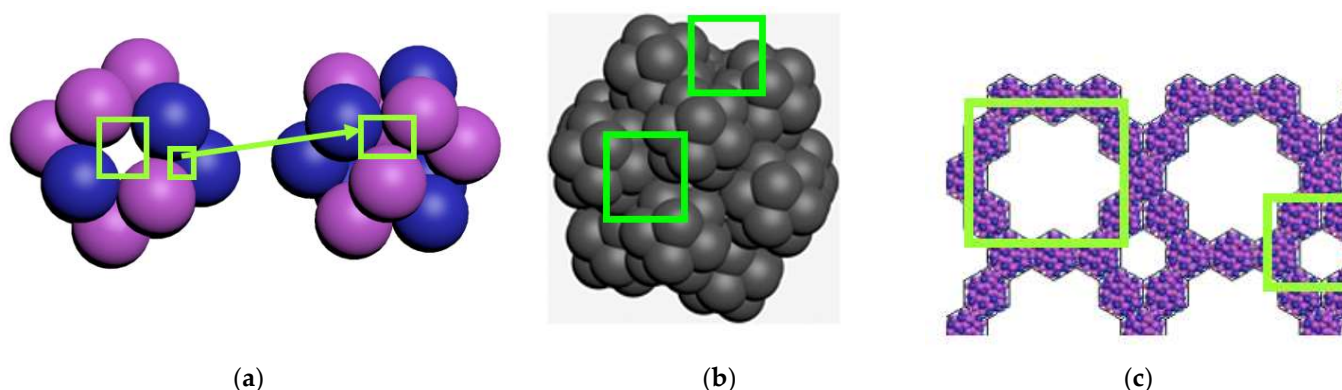


**Figure 27.** Three pore types: (a) type one (micropores); (b) type two (mesopores); (c) type three (macropores) in generalized hierarchical three-dimensional percolation cluster model.

The growth of fractal aggregates (clusters) from sol particles  $\text{SnO}_2$  and  $\text{SiO}_2$  based on the modified models of diffusion-limited and cluster–cluster aggregation was discussed.

The result of the simulation is a visual observation of fractal changes and an understanding of the possibility of varying the value of the flow threshold. Modeling allowed us to explain the high value of the flow threshold in the experiment. It was shown that the nonconducting phase is formed not only due to the formation of the dielectric-phase  $\text{SiO}_2$ , but also due to the formation of mixed-phase  $\text{SnO}_2$  and  $\text{SiO}_2$ .

Two- and three-dimensional percolation models based on experimental data and using simulated fractal clusters of  $\text{SnO}_2$  and  $\text{SiO}_2$  particles were developed in this work. The transition from theoretical problems (which are reduced to finding the value of flow thresholds for two-dimensional lattices) was made to solve experimental problems of percolation theory in a system based on tin and silicon dioxides. The experimental results of the study allowed us to determine the composition of the nanocomposite at which a percolation cluster occurs (50  $\text{SiO}_2$ —50  $\text{SnO}_2$  (mol. %)).

Modeling of  $\text{SnO}_2$  and  $\text{SiO}_2$  particles, which in turn also consist of clusters (the next step in the hierarchy), was performed based on principles for constructing nanoclusters along one tetrahedral and octahedral lines using three-dimensional modeling. Therefore, a generalized hierarchical three-dimensional percolation cluster model is proposed:

1. Micropores formed by the gaps between three or four globules (particles of  $\text{SnO}_2$  and  $\text{SiO}_2$ ) with the circle radius  $\beta$ ;
2. Mesopores formed by the gaps between 13-atom octahedral clusters;
3. Macropores formed by the gaps between the six regular hexagons and macropores formed by the gaps between the twelve regular hexagons.

Thus, we propose a method to assess the surface area, knowing the experimental sizes of macropores (of the third type) and taking into account the micro- and mesopores with sizes below a few nanometers:

1. Estimate the size of macropores (of the third type) in a proposed multimodal model based on an enhanced Kepler net of the 4612 type with hexagonal cells using atomic force microscopy;
2. Estimate the experimental size of the necks between the macropores based on the AFM data;
3. Calculate the radius size of the globule representing the glass-forming net of silicon dioxide by relating the experimental neck size to 7;
4. Calculate the size of the second (mesopores) type of pores using the ratios  $1.4 \beta$  and  $1.1 \beta$ ;

5. Calculate the size of the first (micropores) type of pores using the ratios 0.16  $\beta$  and 0.38  $\beta$ .
6. Construct surface profiles taking into account pore sizes using a multimodal model and calculate surface areas based on the triangulation method.

**Author Contributions:** I.K., technology, methodology, measurements, writing—review and editing; V.M., development of model concepts, review of publications on the topic of the article; P.K., modeling, creation of software products, model construction, illustrations for the article, editing. All authors have read and agreed to the published version of the manuscript.

**Funding:** This research received no external funding.

**Institutional Review Board Statement:** Not applicable.

**Informed Consent Statement:** Not applicable.

**Data Availability Statement:** Not applicable.

**Conflicts of Interest:** The authors declare no conflict of interest.

## References

1. Cölfen, H.; Antonietti, M. *Mesocrystals and Nonclassical Crystallization*; Wiley: Chichester, UK; Hoboken, NJ, USA, 2008; 276p.
2. Jehannin, M.; Rao, A.; Colfen, H. New horizons of nonclassical crystallization. *J. Am. Chem. Soc.* **2019**, *141*, 10120–10136. [[CrossRef](#)]
3. Niederberger, M.; Cölfen, H. Oriented attachment and mesocrystals: Non-classical crystallization mechanisms based on nanoparticle assembly. *Phys. Chem. Chem. Phys.* **2006**, *8*, 3271–3287. [[CrossRef](#)] [[PubMed](#)]
4. Cölfen, H.; Antonietti, M. Mesocrystals: Inorganic superstructures made by highly parallel crystallization and controlled alignment. *Angew. Chem. Int. Ed.* **2005**, *44*, 5576–5591. [[CrossRef](#)] [[PubMed](#)]
5. Sturm, E.V.; Cölfen, H. Mesocrystals: Past, Presence, Future. *Crystals* **2017**, *7*, 207.
6. Shevelkov, A.V. Chemical aspects of thermoelectric materials creation. *Russ. Chem. Rev.* **2008**, *77*, 3–21. [[CrossRef](#)]
7. Kononova, I.E.; Maraeva, E.V.; Skornikova, S.A.; Moshnikov, V.A. Influence of Binder on Porous Structure of Zeolite Compositions and Their Catalytic Activity. *Glass Phys. Chem.* **2020**, *46*, 162–169. [[CrossRef](#)]
8. Madison, A.E. Substitution rules for icosahedral quasicrystals. *RSC Adv.* **2015**, *5*, 5745–5753. [[CrossRef](#)]
9. Madison, A.E.; Madison, P.A. Structure of icosahedral quasicrystals within the multiple cell approach. *Struct. Chem.* **2020**, *31*, 485–505. [[CrossRef](#)]
10. Madison, A.E.; Madison, P.A. Looking for alternatives to the superspace description of icosahedral quasicrystals. *R. Soc. A Math. Phys. Eng. Sci.* **2019**, *475*, 20180667. [[CrossRef](#)]
11. Bobkov, A.A.; Kononova, I.E.; Moshnikov, V.A. Material science of micro- and nanosystems. In *Hierarchical Structures*; Moshnikov, V.A., Ed.; SPbETU 'LETI' Publ.: St. Petersburg, Russia, 2020; Volume 2017, 204p.
12. Kononova, I.E.; Kononov, P.V.; Moshnikov, V.A. Development of a model for the formation of materials with a hierarchical pore structure produced under sol–gel processing conditions. *Inorg. Mater.* **2018**, *54*, 478–489. [[CrossRef](#)]
13. Dubov, P.L.; Korol'kov, D.V.; Petranovskij, V.P. *Klastery i Matrichno-Izolirovannyye Klasternyye Sverhstruktury*; SPb.: Izd-vo SPbGU: Sankt-Peterburg, Russia, 1995; 256p.
14. Kononova, I.; Kononov, P.; Moshnikov, V.; Ignat'ev, S. Fractal-Percolation structure architectonics in sol-gel synthesis. *Int. J. Mol. Sci.* **2021**, *22*, 10521. [[CrossRef](#)] [[PubMed](#)]
15. Spivak, Y.M.; Kononova, I.E.; Kononov, P.V.; Moshnikov, V.A.; Ignat'ev, S.A. The architectonics features of heterostructures for ir range detectors based on polycrystalline layers of lead chalcogenides. *Crystals* **2021**, *11*, 1143. [[CrossRef](#)]
16. Smerdov, R.; Mustafaev, A.; Spivak, Y.; Moshnikov, V. Functionalized nanostructured materials for novel plasma energy systems. In *Topical Issues of Rational Use of Natural Resources 2019*; CRC Press: Boca Raton, FL, USA, 2019; pp. 434–441.
17. Smerdov, R.; Spivak, Y.; Bizyaev, I.; Somov, P.; Gerasimov, V.; Mustafaev, A.; Moshnikov, V. Advances in Novel Low-Macroscopic Field Emission Electrode Design Based on Fullerene-Doped Porous Silicon. *Electronics* **2020**, *10*, 42. [[CrossRef](#)]
18. Tomaev, V.; Levine, K.; Stoyanova, T.; Syrkov, A.G. Synthesis and Study of a Polypyrrole–Aluminum Oxide Nanocomposite Film on an Aluminum Surface. *Glas. Phys. Chem.* **2019**, *45*, 291–297. [[CrossRef](#)]
19. Krasnyy, V.A. The use of nanomaterials to improve the wear resistance of machine parts under fretting corrosion conditions. In *IOP Conference Series: Materials Science and Engineering*; IOP Publishing: Bristol, UK, 2019; Volume 560, p. 012186. [[CrossRef](#)]
20. Salikhov, K.M.; Stoyanov, N.D.; Stoyanova, T.V. Using Optical Activation to Create Hydrogen and Hydrogen-Containing Gas Sensors. *Key Eng. Mater.* **2020**, *854*, 87–93. [[CrossRef](#)]
21. Tomaev, V.V.; Levine, K.L.; Stoyanova, T.V.; Sirkov, A.G. Formation of nanocomposite film (polypyrrol)/(aluminum) oxide on aluminum surface. In *AIP Conference Proceedings*; AIP Publishing LLC: Melville, NY, USA, 2019; Volume 2064, p. 030016.
22. Gasanly, S.A.; Tomaev, V.V.; Stoyanova, T.V. The concept of the phases ratio control during the formation of composite filamentary nanocrystals  $x\text{InSe}-(1-x)\text{In}_2\text{O}_3$  on glass substrates. *J. Phys. Conf. Ser.* **2017**, *917*, 32021. [[CrossRef](#)]

23. Syrkov, A.G. On the priority of Saint-Petersburg Mining University in the field of nanotechnology science and nanomaterials. *J. Min. Inst.* **2016**, *221*, 730–736.
24. Pleskunov, I.V.; Syrkov, A.G. Razvitie issledovanij nizkorazmernyh metallosoderzhashchih si-stem ot P.P.Vejmarna do nashih dnei. *J. Min. Inst.* **2018**, *231*, 287.
25. Wang, J.; Mbah, C.F.; Przybilla, T.; Apeleo Zubiri, B.; Spiecker, E.; Engel, M.; Vogel, N. Magic number colloidal clusters as minimum free energy structures. *Nat. Commun.* **2018**, *9*, 5259. [[CrossRef](#)]
26. Kaatz, F.H.; Bultheel, A. Magic Mathematical Relationships for Nanoclusters. *Nanoscale Res. Lett.* **2019**, *14*, 150. [[CrossRef](#)]
27. Reimann, S.M.; Koskinen, M.; Häkkinen, H.; Lindelof, P.E.; Manninen, M. Magic triangular and tetrahedral clusters. *Phys. Rev. B* **1997**, *56*, 1247–1250. [[CrossRef](#)]
28. Harbola, M.K. Magic numbers for metallic clusters and the principle of maximum hardness. *Proc. Natl. Acad. Sci. USA* **1992**, *89*, 1036–1039. [[CrossRef](#)]
29. Jia, Y.; Yu, X.; Zhang, H.; Cheng, L.; Luo, Z. Tetrahedral Pt 10–Cluster with Unique Beta Aromaticity and Superatomic Feature in Mimicking Methane. *J. Phys. Chem. Lett.* **2021**, *12*, 5115–5122. [[CrossRef](#)] [[PubMed](#)]
30. Ignatiev, S.A.; Folomkin, A.I.; Tretiakova, Z.O.; Glazunov, K.O. Moodle e-Learning Platform as an effective tool for teaching descriptive geometry in conditions of the COVID-19 pandemic. *Geom. Graph.* **2020**, *3*, 52–67.
31. Lu, X.; Hasegawa, G.; Kanamori, K.; Nakanishi, K. Hierarchically porous monoliths prepared via sol–gel process accompanied by spinodal decomposition. *J. Sol-Gel Sci. Technol.* **2020**, *95*, 530–550. [[CrossRef](#)]
32. Lu, X.; Kanamori, K.; Nakanishi, K. Synthesis of hierarchically porous MgO monoliths with continuous structure via sol–gel process accompanied by phase separation. *J. Sol-Gel Sci. Technol.* **2019**, *89*, 29–36. [[CrossRef](#)]
33. Brinker, C.J. Hydrolysis and condensation of silicates: Effects on structure. *J. Non-Cryst. Solids* **1988**, *100*, 31–50. [[CrossRef](#)]
34. Brinker, C.J.; Scherer, G.W. Sol-Gel Science. In *The Physics and Chemistry of Sol-Gel Processing*; Academic Press: San Diego, CA, USA, 1990.
35. Boilot, J.P.; Colomban, P.; Blanchard, N. Formation of superionic gels and glasses by low temperature chemical polymerization. *Solid State Ion.* **1983**, *9–10*, 639–643. [[CrossRef](#)]
36. Jullien, R.; Botet, R. *Aggregation and Fractal Aggregates*; World Scientific Publishing Company: Singapore, 1987; 130p.
37. Beelen, T.P. Inorganic particle gels. *Curr. Opin. Colloid Interface Sci.* **1996**, *1*, 718–725. [[CrossRef](#)]
38. Gheonea, R.; Crasmareanu, E.C.; Plesu, N.; Saucă, S.; Simulescu, V.; Ilia, G. New Hybrid Materials Synthesized with Different Dyes by Sol-Gel Method. *Adv. Mater. Sci. Eng.* **2017**, *2017*, 4537039. [[CrossRef](#)]
39. Abrashova, E.V.; Gracheva, I.E.; Moshnikov, V.A. Functional nanomaterials based on metal oxides with hierarchical structure. *J. Phys. Conf. Ser.* **2013**, *461*, 012019. [[CrossRef](#)]
40. Kononova, I.E.; Moshnikov, V.A.; Krishtab, M.; Pronin, I.A. Fractally aggregated micro- and nanosystems synthesized from sols. *Glass Phys. Chem.* **2014**, *40*, 190–202. [[CrossRef](#)]
41. Gracheva, I.E.; Moshnikov, V.; Maraeva, E.; Karpova, S.S.; Aleksandrova, O.A.; Alekseyev, N.I.; Kuznetsov, V.V.; Olchowik, G.; Semenov, K.; Startseva, A.V.; et al. Nanostructured materials obtained under conditions of hierarchical self-assembly and modified by derivative forms of fullerenes. *J. Non-Cryst. Solids* **2012**, *358*, 433–439. [[CrossRef](#)]
42. Moshnikov, V.; Gracheva, I.E.; Kuznezov, V.V.; Maximov, A.; Karpova, S.S.; Ponomareva, A.A. Hierarchical nanostructured semiconductor porous materials for gas sensors. *J. Non-Cryst. Solids* **2010**, *356*, 2020–2025. [[CrossRef](#)]
43. Moshnikov, V.A.; Gracheva, I.; Lenshin, A.S.; Spivak, Y.M.; Anchkov, M.G.; Kuznetsov, V.V.; Olchowik, J.M. Porous silicon with embedded metal oxides for gas sensing applications. *J. Non-Cryst. Solids* **2012**, *358*, 590–595. [[CrossRef](#)]
44. Zha, W.; Yan, S.; Li, D.; Lu, D. A study of correlation between permeability and pore space based on dilation operation. *Adv. Geo-Energy Res.* **2017**, *1*, 93–99. [[CrossRef](#)]

**Disclaimer/Publisher’s Note:** The statements, opinions and data contained in all publications are solely those of the individual author(s) and contributor(s) and not of MDPI and/or the editor(s). MDPI and/or the editor(s) disclaim responsibility for any injury to people or property resulting from any ideas, methods, instructions or products referred to in the content.